Modeling of the Large Torsional Deformation of an Extremely Flexible Rotor in Hover

Jérôme Sicard* and Jayant Sirohi†
University of Texas at Austin, Austin, Texas 78712

This paper describes the refined modeling of the large torsional deformation of extremely flexible rotor blades with negligible structural stiffness. Equations of motion including flap bending and torsion, specifically tailored toward unconventional blades with a tip mass and experiencing large elastic twist angles, are derived using the extended Hamilton's principle. In particular, the foreshortening of the twisted blade arising from the trapeze effect (also called bifilar effect) is explicitly included. Quasi-steady aerodynamic forces are calculated using the blade element momentum theory. The nonlinear coupled equations of motion are solved using a finite-element method. The analysis is used to predict the thrust as well as the spanwise distribution of flap bending and twist of an 18-in.-diam rotor with extremely flexible blades rotating at 1200 rpm at various collective pitch angles. These predictions are correlated with the measurement of loads obtained using a load cell, and the measurement of the deformation obtained using a noncontact optical technique called digital image correlation. It is found experimentally and analytically that tip twist angles in the range of 10 to 40 deg, depending on the blade design, are attained. This torsional deformation is dictated by the combined action of the propeller moment and the trapeze effect. A detailed explanation of the contribution of the trapeze effect to the equations of motion is presented, and it is shown that omitting the axial foreshortening due to the trapeze effect leads to a 50% error in the computation of blade-tip twist.

Nomenclature

A, A_m	=	blade and tip mass cross-sectional area, respectively
B_1, B_2, B_3	=	blade cross-sectional integral constants
C_a	=	blade camber
C_l	=	lift coefficient
C_m	=	pitching moment coefficient
c	=	blade chord
D	=	drag force
d_η, d_ξ	=	chordwise and flatwise offsets of mass centroid of blade cross section from elastic axis (positive when in front of elastic axis)
E	=	Young's modulus
e_η, e_ξ	=	chordwise and flatwise offsets of area centroid of blade cross section from elastic axis (positive when in front of elastic axis)
F_Z	=	resultant of the aerodynamic forces along the Z axis
G	=	shear modulus
g	=	gravitational acceleration
$H_i^0(x), H_i^1(x)$	=	Hermite cubic polynomials
I_ξ, I_η	=	blade area moments of inertia about η and ξ axes, respectively
$I_{\eta\xi}$	=	blade area product of inertia
J	=	blade polar moment of inertia
K^i	=	Jacobian matrix at the ith iteration
k_A	=	polar radius of gyration of blade cross-sectional area about elastic axis
k_m	=	polar radius of gyration of blade cross-sectional mass about elastic axis
k_{m_ξ}, k_{m_η}	=	mass radii of gyration about η and ξ axes, respectively
k_β	=	torsional flapping spring stiffness
L	=	lift force
$L_i(x)$	=	Lagrange quadratic polynomials
L_1, L_2	=	distances between tip mass ends and tip mass attachment point
M	=	number of degrees of freedom
M_ϕ	=	resultant of the aerodynamic moments about the elastic axis
m_0, m_T	=	blade mass and tip mass per unit length, respectively
N	=	number of finite elements
q_i	=	elemental vector of generalized coordinates
R	=	rotor radius
R^i	=	residue vector at the ith iteration
Re_c	=	chord Reynolds number
r_0, r_1	=	position vector of a blade particle before and after deformation, respectively, projected in the $\{X, Y, Z\}$ reference frame
T	=	kinetic energy
T_0	=	time-invariant kinetic energy
t	=	blade thickness
U	=	strain energy
U_P	=	air velocity of blade section, perpendicular to the disk plane
U_T	=	air velocity of blade section, tangent to the disk plane
u_F	=	radial foreshortening of the elastic axis
u^i	=	global displacement vector at the ith iteration
V	=	potential energy
V_g	=	gravitational potential energy
W_a	=	work done by aerodynamic forces
W_{nc}	=	work done by nonconservative forces
w	=	flap bending deflection
$\{X_I, Y_I, Z_I\}$	=	inertial reference frame
$\{X, Y, Z\}$	=	hub fixed reference frame
$\{X, Y_T, Z_T\}$	=	tip mass fixed reference frame
$\{X, \eta, \xi\}$	=	blade fixed reference frame
x_A	=	aerodynamic center offset from elastic axis (positive when in front of elastic axis)

*Graduate Research Assistant, Department of Aerospace Engineering and Engineering Mechanics; jerome.sicard@utexas.edu. Student Member AIAA.
†Assistant Professor, Department of Aerospace Engineering and Engineering Mechanics; jayant.sirohi@mail.utexas.edu. Senior Member AIAA.

x_0	=	blade root cutout
ϵ_{ij}	=	strain tensor in a Lagrangian sense
ϵ	=	parameter of the order of the normalized flap bending deflection
η_T, ξ_T	=	chordwise and flatwise offsets of tip mass attachment point from elastic axis (positive when in front of elastic axis)
θ	=	local pitch angle
θ_0	=	collective pitch angle
θ_{ind}	=	index angle between tip mass longitudinal axis and blade chord
λ^i	=	line-search algorithm constant at the ith iteration
ν_β	=	rotating flap frequency
ν_θ	=	rotating torsional frequency
ρ, ρ_m	=	blade and tip mass density, respectively
σ	=	rotor solidity
ϕ	=	elastic twist angle
χ, λ	=	bound variables
ψ	=	induced angle of attack
Ω	=	rotational speed

Subscripts

b, m	=	quantity corresponding to the blade and the tip mass, respectively
R	=	quantity is evaluated at blade tip

Superscript

| ′	=	space derivative

I. Introduction

ROTARY-WING micro aerial vehicles (MAVs) have become increasingly popular over the past decade because they are capable of performing missions that conventional manned vehicles or larger unmanned aerial vehicles cannot [1–3]. Specifically, their unique ability to take off and land vertically, hover, and fly at very low advance ratios makes them perfectly suited to indoor surveillance or reconnaissance missions. Flight in these cluttered environments poses several challenges, such as increased danger of blade impact with obstacles and limited access to confined areas due to the large rotor diameter.

The extremely flexible morphing rotor was proposed as a potential solution to some of these issues. This rotor features blades that are so flexible that they can be rolled up and stowed in the rotor hub. In this way, the rotor diameter can be changed in flight; increasing the diameter can increase the hover endurance and decreasing the diameter can allow access to confined spaces. The full retraction of the blades is also advantageous for storage and ground transportation of the MAV. Furthermore, the probability of survival of the vehicle upon collision with an object is increased by the high compliance of the rotor blades. In such an event, the rotor blade can experience large deformations and elastically recover its original shape. Sicard and Sirohi [4] designed and tested several prototypes of 18-in.-diam extremely flexible rotors in hover.

The prototypes featured constant chord blades with a thin circular-arc airfoil section. The blades were fabricated using a carbon-fiber composite with a polyurethane epoxy resin. By choosing resins of different shear stiffness and by varying the orientation of the composite plies, rotor blades with different bending and torsional flexibility were realized. A two-bladed rotor with blades that are extremely flexible in flap bending and torsion is shown in Fig. 1a. Elastic flexibility in flap bending does not have a major impact on the behavior of the rotor due to the stiffening effect of centrifugal forces (as in the case of an articulated rotor, for example). However, torsional flexibility plays a key role in the steady-state as well as dynamic behavior of a rotor blade. Decreasing the torsional stiffness makes a rotor blade prone to pitch–flap flutter. Therefore, the flexible rotor blade featured a tip mass designed to provide stiffness and

a) Flexible rotor at rest, mounted on hover test stand
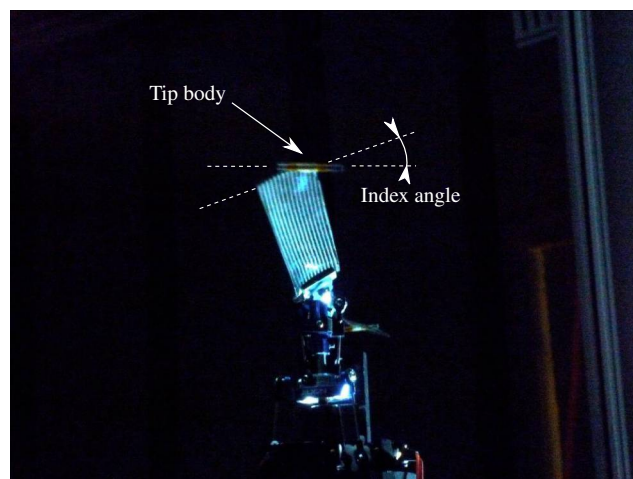
b) Flexible blade rotating at 1500 RPM

Fig. 1   18-in.-diam rotor (design BP) with extremely flexible blades [4].

stabilization through the action of centrifugal forces. However, the propeller moments acting on the rotor blade and tip mass induced a large, spanwise negative twist. Although a limited amount of negative twist, on the order of 12 to 15 deg per rotor radius, can be favorable for the hover efficiency of a microhelicopter [5], Sicard and Sirohi [4] showed that flexible blades experienced twist rates of up to 40 deg per rotor radius at high blade loading, leading to poor figures of merit. They experimentally investigated several designs of torsionally soft rotors by varying the orientation of the tip mass. They showed that the negative induced twist could be alleviated by orienting the tip mass chordwise and introducing an index angle between the blade chord and the minor principal axis of inertia of the tip body. This blade, termed as the "design BP", is shown rotating at 1500 rpm in Fig. 1b. Further optimization of the flexible rotor requires accurate prediction of its deformation given a set of geometrical parameters.

The objective of this paper is to describe an aeroelastic analysis specifically developed to model the large, steady-state deformation of a torsionally soft rotor. This model can be used to analytically explore the effect of design parameters on these unconventional rotor blades, with the goal of optimizing specific performance metrics.

II. State of the Art and Present Approach

The analytical study of rotating beams has sparked a great deal of interest throughout the second half of the last century, particularly to support the development of rotorcraft aeromechanics analyses. One of the initial studies was conducted by Houbolt and Brooks [6] who

derived the partial differential equations of motion for the coupled bending and torsion of twisted nonuniform beams using a linear analysis. As the significance of nonlinear terms in the aeroelasticity of rotary-wings was discovered, nonlinear equations of motion for combined flap bending, lead–lag bending, torsion, and extension of twisted nonuniform rotor blades were derived independently by several authors [7–9]. These theories, based on truncation schemes and accurate to second order, relied on the restriction that normalized bending deflections and angles of twist were small with respect to unity. The equations of motion were derived assuming a displacement field, and the rotor blades were modeled as beam elements for which the cross-sectional constants were calculated at the elastic axis. Then, in the mid-1990s, studies addressing the arbitrarily large displacements and rotations of composite rotor blades were derived, using a geometrically exact beam theory [10,11] or a multibody formulation [12]. Nowadays, most modern rotor blade aeromechanics analyses stem from one of these two approaches. More details on the development of structural dynamics modeling of rotor blades can be found in a review by Datta et al. [13] and a report by Johnson [14].

Although it is understood that the deformation of rotor blades with negligible structural stiffness can be accurately predicted using an analysis valid for large displacements and large rotations (see Hodges [11] or Bauchau and Kang [12] for instance), the purpose of the present work is to show that good predictions can be obtained by using a model based on a Hamiltonian formulation along with an appropriate ordering scheme, including typical physical effects associated with large angles of twist. In particular, for blades that are extremely flexible in torsion, the elastic twist angles can be large, and the trapeze effect becomes important. A limited number of aeroelastic analyses have been developed in the past to specifically address rotor blades with negligible structural stiffness. Goldman [15] and Winston [16,17] analyzed and tested flexible rotor blades constructed of a thin fabric airfoil supported by cables at the leading and trailing edges. Preliminary stability results were obtained using a simplified analytical model and assuming the first coupled flapwise bending and torsional mode shapes of the blade.

The present paper has two goals. The first objective is to demonstrate how an aeroelastic analysis with two degrees of freedom (flap bending and twist), and whose equations are truncated consistently with an ordering scheme, can accurately predict the deformations of a rotor blade with negligible torsional stiffness. The second objective is to investigate the importance of the terms arising from the trapeze effect for torsionally soft rotors and their contribution to the calculated twist and overall deflection predictions. Accordingly, the nonlinear, steady-state aeroelastic equations for combined flap bending and twist of a rotor blade are derived. Throughout the derivation, special attention is given to the terms associated with large twist angles. In particular, the truncation scheme is chosen such that the elastic twist angle is considered to be of the same order of magnitude as the collective pitch angle. In addition, the foreshortening due to the trapeze effect is explicitly included. The analysis also includes the kinetic and potential energies of a tip body that is required to ensure stability. The equations of motion are solved using the finite-element method. Analytical predictions of flap bending and twist deformation are correlated with measurements obtained using a noncontact, optical technique called digital image correlation [18,19].

III. Experimental Setup

A digital image correlation (DIC) system was used to measure the deformation of the flexible rotor blades spinning at 1200 rpm on a hover test stand.

A. Digital-Image-Correlation Measurement Setup

DIC is a noncontact, optical measurement technique that combines photogrammetry and image correlation. In the DIC technique, two digital cameras are arranged to capture stereoscopic images of an object. The positions of the cameras are calibrated with a target of known geometry, yielding a photogrammetric mapping function. Images of the object are captured before and after loads are applied. Cross-correlation of the images, along with the mapping function,

yields a three-dimensional deformation map of the object. Details of this technique applied to measure rotor blade deformation are given in [18,19]. From the DIC measurements, the spanwise distribution of flap bending of the rotor blade elastic axis as well as the elastic twist were extracted.

In the present study, the flexible rotor was tested in hover, on a 1.2-m-tall rotor test stand (Fig. 2), designed and fabricated in-house (see details in [4]). Two digital cameras, Imager ProX 2M charge-coupled-device (CCD) cameras, were arranged so that they focus on a rotor blade at a specific azimuthal angle. Each camera had a resolution of 1600×1200 pixels, a maximum imaging frequency of 29.9 frames per second, and an exposure time varying from 500 ns to 1000 s. Their 14 bit CCD sensor had a sensitivity of 16,384 gray levels. The lenses mounted on the cameras were Nikon AF Nikkor 50 mm $f/1.8D$, with an aperture varying between $f/1.8$ and $f/22$. A Scheimpflug adapter was also added to the lens to keep the entire rotor blade span in focus. A signal from a 1/rev sensor on the rotor shaft was used to synchronize the image capture with the rotor rotation. This signal was also sent to a 10 W xenon stroboscope, effectively illuminating the rotor once per revolution. The camera shutters were kept open over several rotor revolutions, creating multiple exposures of the rotor blade on the CCD sensor. The capture of multiple exposures resulted in a higher-intensity image than possible with only one exposure of the rotor blade. A commercially available DIC software (LaVision DaVis 7.2 — StrainMaster 3D) was used to process the images and to calculate surface heights as well as deformation maps. A postprocessor written in-house was used to extract the flap bending and torsional deformations along the blade span. The rotor test stand also featured a six-component strain gauge load cell (ATI Mini40E), with a full-scale rating of 5 lb in the thrust direction, that continuously recorded rotor forces and moments in the fixed frame.

B. Flexible Rotor

The flexible rotor blades used in this study were fabricated out of composite material comprising two plies of a carbon-fiber fabric (CST CF-131-1k, 2.9 oz/yd² 0/90 deg plain weave) and a
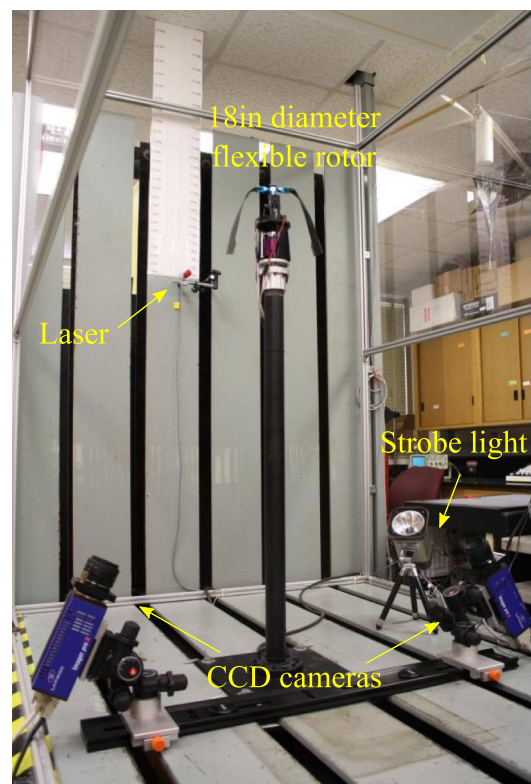

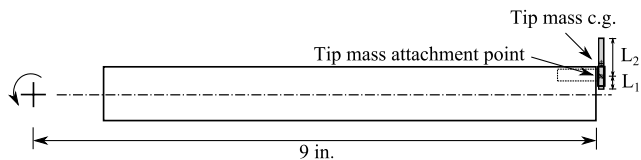**Fig. 2   Hover test stand equipped with CCD cameras, stroboscope, and laser for root pitch angle measurement.**

Fig. 3   Planform of flexible-blade BP.

Fig. 4   High-contrast random pattern on the bottom surface of flexible rotor blade.

polyurethane matrix (Aircraft Spruce AlphaPoxy). Each ply was arranged such that the fibers of the cloth made an angle of $+45/-45$ deg relative to the blade span. This combination of ply orientation and material shear modulus was found to be the most favorable to reel the blade into a cylinder with minimal radius of curvature. Although the choice of the matrix resulted in a blade soft in torsion, the angle of the fibers lowered the bending stiffness to accommodate the roll-up of the blade. The composite was cured at room temperature in a compression mold that had the desired airfoil shape and blade planform. The blades had a constant chord, thin circular-arc airfoil section, and a chordwise-oriented cylindrical mass attached at the blade tip (see Fig. 3; this design is labeled as blade BP in [4]). The chordwise position of the tip mass attachment point could be adjusted between the two rod ends, varying the lengths L_1 and L_2. A two-bladed rotor was created by attaching the flexible blades to a rigid hub. Table 1 summarizes the parameters of the flexible rotor. Normalized flap bending stiffness, lead–lag bending stiffness, and torsional stiffness are shown in Table 2. For comparison, the normalized torsional stiffness of a blade having the same cross section but fabricated out of AGP370-5H/3501 carbon-fiber composite is equal to 6.64. Therefore, the low-shear-modulus polyurethane matrix results in a decrease in torsional stiffness by three orders of magnitude. Also shown in Table 2 are the first rotating torsional and flap frequencies of the extremely flexible blade. Note that a clamped condition of the pitch degree of freedom at the root, as it is imposed in the present study, typically leads to high torsional frequencies for conventionally stiff, full-scale rotor blades. However, it can be seen in Table 2 that the rotating torsional frequency of the flexible rotor blade is on the order of 3.3/rev.

The bottom surface of each blade was painted with a high-contrast random speckle pattern for the DIC measurements (Fig. 4). The

speckle size ranged from approximately 0.15 to 1.95 mm, chosen for optimum accuracy based on the resolution of the digital cameras used in DIC.

IV.   Analytical Model

The analytical model was derived using the extended Hamilton's principle. A structural model based on engineering beam theory was used to determine the kinetic energy and strain energy of the rotor blade as well as the tip mass. The blade deformation was assumed to have only two degrees of freedom: flap bending and torsion. Extensional elongation was neglected; however, the axial displacement, or foreshortening of the elastic axis, induced by the combined action of bending and torsion, was explicitly included. Coordinate systems were defined with respect to the undeformed and deformed positions of the blade, and an ordering scheme was proposed to eliminate higher-order terms. The aerodynamic model included only quasi-steady forcing terms. Finally, the equations of motion were solved using the finite-element method.

The extended Hamilton's principle states that
If

$$\delta q_i|_{t_1} = \delta q_i|_{t_2} = 0, \quad \text{for } i = 1, \ldots, M$$

then

$$\int_{t_1}^{t_2} (\delta T - \delta V + \delta W_{\text{nc}}) \, \mathrm{d}t = 0 \qquad (1)$$

where δq_i are the generalized coordinates; δT and δV are the variations of kinetic and potential energies, respectively; and δW_{nc} is the virtual work done by nonconservative forces. By retaining only time-invariant terms, and including the kinetic and potential energy associated with a tip mass, we obtain the equation governing the static (or steady-state) equilibrium of the rotor blade:
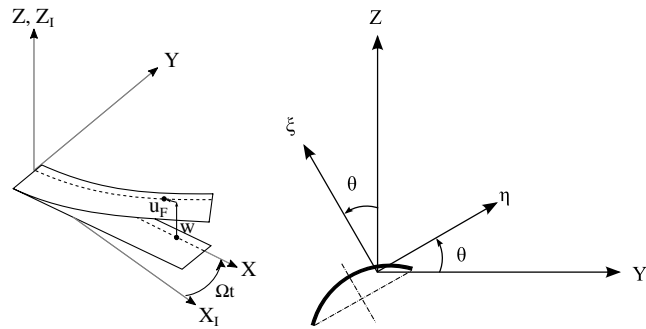
$$(\delta T_0 - \delta U - \delta V_g + \delta W_a)_b + (\delta T_0 - \delta V_g)_m = 0 \qquad (2)$$

where δT_0, δU, and δV_g are the variations of time-invariant kinetic energy, strain energy, and gravitational potential energy, respectively. δW_a is the virtual work done by aerodynamic forces. The subscripts b and m indicate the quantities corresponding to the blade and the tip mass, respectively.

A.   Coordinate System

Three coordinate systems were used in the present analysis. Figure 5a shows the schematic of a rotor blade before and after flap bending and torsional deformation. $\{X_I, Y_I, Z_I\}$ is an inertial reference frame. $\{X, Y, Z\}$ is attached to the undeformed position of the blade, with X coincident with the elastic axis and Z aligned with the rotor shaft. Finally, $\{X, \eta, \xi\}$ (Fig. 5b) is attached to the circular-arc airfoil cross section, rotated by the angle θ with respect to $\{X, Y, Z\}$.

Throughout this analysis, the flap bending deflection w was defined as the displacement, projected on the Z axis, of points located along the elastic axis of the blade. The local pitch angle θ was the sum of the blade collective pitch θ_0 and the local elastic twist ϕ:

Table 1   Flexible rotor parameters

Airfoil	Circular arc
Rotor radius R, in. (m)	9 (0.229)
Root cutout x_0, in. (m)	2.323 (0.059)
Chord c, in. (m)	0.9 (0.023)
Camber C_a, % of c	7.5
Thickness t, % of c	1.39
Rotor solidity σ	0.064
Total mass m, oz (g)	0.160 (4.53)
Mass per unit length (m_0), oz $\cdot$ in.$^{-1}$ (kg $\cdot$ m^{-1})	0.0116 (0.013)
Tip mass m_T, oz (g)	0.072 (2.03)
Length of the tip mass L_T, in. (m)	1 (0.0254)
Chordwise coordinate of the tip mass attachment point (η_T), % of c	12
Tip mass end offset from attachment point (L_1), % of L_T	30
Rotational speed Ω, rpm	1200
Tip Reynolds number Re_c	46,160

Table 2   Flexible-blade normalized stiffnesses

Flap bending stiffness	$\frac{EI_\eta}{m_0\Omega^2 R^4}$	9.65×10^{-2}
Lead–lag bending stiffness	$\frac{EI_\xi}{m_0\Omega^2 R^4}$	2.54×10^{1}
Torsional stiffness	$\frac{GJ}{m_0\Omega^2 R^4}$	1.00×10^{-3}
First rotating torsional frequency, /rev	ν_θ	3.3
First rotating flap frequency, /rev	ν_β	1.1

a) Blade coordinate systems   b) Cross-section coordinate systems

Fig. 5   Coordinate systems.

$$\theta(x) = \theta_0 + \phi(x) \tag{3}$$

B. Structural Model

The structural model of the rotor blade was based on engineering beam theory. Kinetic and potential energies of the rotor blade as well as tip mass were found based on the deformations, in conjunction with an ordering scheme. The key aspect of the structural model is the inclusion of the trapeze effect due to the low torsional stiffness of the rotor blade.

1. Trapeze Effect

Conventional helicopter rotor blades are relatively stiff in torsion, due to the skin of the blade acting as a closed torque box. The flexibility in torsion is due predominantly to the control system stiffness. Therefore, propeller moments dominate the torsional deformation of a conventional blade. In contrast, the flexible rotor blade under consideration has a thin circular-arc airfoil and is composed of a carbon-fiber composite with a low-shear-modulus matrix. Consequently, the flexible blade has a very low torsional stiffness, and twisting of the rotor blade results in a kinematic radial foreshortening. This nonlinear effect is called the trapeze (or bifilar) effect [20]. It plays an important role in the torsional dynamics of a flexible rotor. The relation between the angle of twist and the induced radial displacement can be illustrated by considering the case of a rotor blade composed of two inextensible cables at the leading and trailing edges, connected at the tip by a rigid link, as shown in Fig. 6.

The Pythagorean theorem applied to Fig. 6b gives

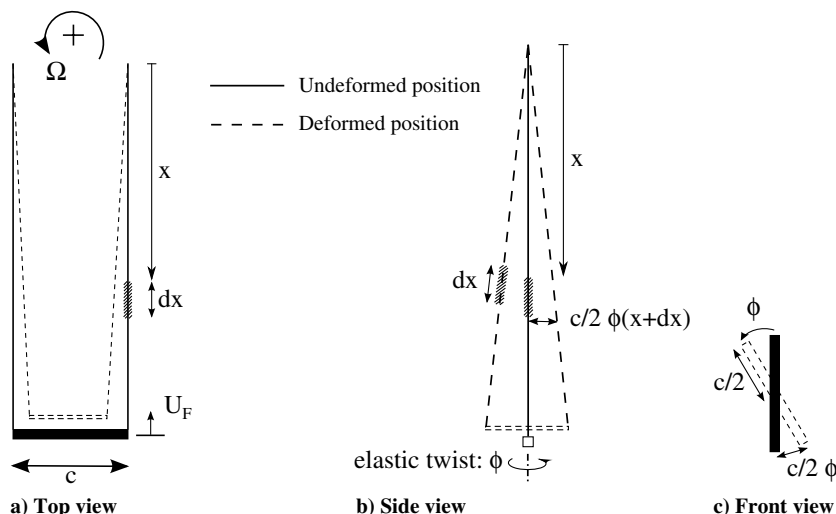$$dx^2 = \left[\frac{c}{2}\phi(x+dx) - \frac{c}{2}\phi(x)\right]^2 + [dx + u_F(x) - u_F(x+dx)]^2 \tag{4}$$

Dividing through by dx and applying the Taylor–Lagrange expansion for small ϕ', we get

$$u_F' = 1 - \left(1 - \frac{c^2}{8}\phi' + O(\phi'^2)\right) \tag{5}$$

Integration along the blade span leads to the radial foreshortening due to twist:

$$u_F = \int_0^x \frac{c^2}{8}\phi'^2 \, dx \tag{6}$$

Although this expression will vary depending on the exact geometry of the rotor blade, we assume it to hold for the present case.

2. Ordering Scheme

As the Hamilton principle is applied [Eq. (2)], it is important to verify that the orders of approximation of the kinetic and potential energies, as well as the work done by nonconservative forces, are the same. Along the lines of previous studies [7–9], we defined an ordering scheme, where each physical quantity was compared to the normalized flap bending deflection w/R, assumed to be of order ϵ. However, in the present analysis, the elastic twist angle ϕ was assumed to be of the same order as the collective pitch angle θ_0 (i.e., of order 1). The ordering scheme is summarized in Table 3.

3. Strain Energy

The general formulation for the variation of the rotor blade strain energy is

$$(\delta U)_b = \int_R \iint_A (E\epsilon_{xx}\delta\epsilon_{xx} + 4G\epsilon_{x\eta}\delta\epsilon_{x\eta} + 4G\epsilon_{x\xi}\delta\epsilon_{x\xi}) \, d\eta \, d\xi \, dx \tag{7}$$

The integrand is a function of the strain tensor $[\epsilon]$ associated with the flap bending and torsional deformation of the rotor blade, which can be defined in a Lagrangian sense as

$$d\boldsymbol{r}_1 \cdot d\boldsymbol{r}_1 - d\boldsymbol{r}_0 \cdot d\boldsymbol{r}_0 = 2\{dxd\eta d\xi\}[\epsilon]\{dxd\eta d\xi\}^T \tag{8}$$

where dx, $d\eta$, and $d\xi$ are increments along the elastic axis and the cross-section axes of the blade in its undeformed position. $d\boldsymbol{r}_0$ and $d\boldsymbol{r}_1$ are the differentials of the position vectors $\boldsymbol{r}_0$ and $\boldsymbol{r}_1$ of a blade particle in the undeformed and deformed configurations, respectively, projected in the $\{X, Y, Z\}$ reference frame. A very detailed derivation of these position vectors is shown in [8,21], and it can be

a) Top view   b) Side view   c) Front view

Fig. 6   Torsion of a rotor composed of two cables and a rigid tip body.

Table 3 Ordering scheme

Term	Order
$\frac{x}{R}, \theta_0, \phi, \frac{\partial}{\partial x}, \frac{\partial}{\partial t}$	$\mathcal{O}(1)$
$\frac{w}{R}, \frac{\eta}{R}, \frac{\xi}{R}, \frac{c}{R}, \frac{\eta_T}{R}, \frac{\xi_T}{R}$	$\mathcal{O}(\epsilon)$
$\frac{E}{m_0 \Omega^2}, \frac{G}{m_0 \Omega^2}$	$\mathcal{O}(\epsilon^{-2})$

shown that the differences resulting from the order in which the flap and pitch transformations are imposed vanish under an appropriate change of variables [21]. For the present case, a "flap–pitch" sequence was chosen, and the position vectors are

$$r_0 = \begin{Bmatrix} x_0 \\ y_0 \\ z_0 \end{Bmatrix} = \begin{Bmatrix} x \\ \eta \cos \theta_0 - \xi \sin \theta_0 \\ \eta \sin \theta_0 + \xi \cos \theta_0 \end{Bmatrix} \quad (9)$$

and

$$r_1 = \begin{Bmatrix} x_1 \\ y_1 \\ z_1 \end{Bmatrix} = \begin{Bmatrix} x - u_F - w'[\eta \sin \theta + \xi \cos \theta] \\ \eta \cos \theta - \xi \sin \theta \\ w + \left(1 - \frac{w'^2}{2}\right)[\eta \sin \theta + \xi \cos \theta] \end{Bmatrix} \quad (10)$$

where u_F is the radial displacement due to flap bending and torsional foreshortening, given by

$$u_F(x) = \int_0^x \left(\frac{w'^2}{2} + \frac{c^2}{8}\phi'^2\right) dx \quad (11)$$

Substituting the position vector relations into Eq. (8), we obtain the following radial and in-plane shear strains:

$$\epsilon_{xx} = -w''(\eta \sin \theta + \xi \cos \theta) + \frac{\phi'^2}{2}(\eta^2 + \xi^2) - \frac{c^2}{8}\phi'^2 + O(\epsilon^4) \quad (12)$$

$$\epsilon_{x\eta} = -\frac{\phi'\xi}{2} + O(\epsilon^3) \quad (13)$$

$$\epsilon_{x\xi} = \frac{\phi'\eta}{2} + O(\epsilon^3) \quad (14)$$

The first term in ϵ_{xx} is the typical component of strain proportional to w'', associated with flap bending. On the neutral axis, this term equals zero. Similarly, for an untwisted blade and no collective pitch, this component of the strain vanishes on any point along $\xi = 0$. The second and third terms account for the normal strains that arise when the rotor blade is twisted. The third term does not appear in studies [7–9]. In these studies, it is instead implicitly included to the axial displacement degrees of freedom (u).

Given the form of the strain tensor, and replacing the integrals over the blade cross section by the constants defined in Table A1, we can write the variation of strain energy as

$$(\delta U)_b = \int_{x_0}^R \Bigg\{ \left[EI_\xi \sin^2 \theta + EI_\eta \cos^2 \theta + EI_{\eta\xi} \sin 2\theta\right] w''$$

$$- \left(\frac{EB_2}{2} \sin \theta + \frac{EB_3}{2} \cos \theta\right) \phi'^2$$

$$+ EA\frac{c^2}{8}\phi'^2 \left(e_\eta \sin \theta + e_\xi \cos \theta\right) \Bigg\} \delta w''$$

$$+ \left\{ \frac{1}{2}(EI_\xi - EI_\eta) w''^2 \sin 2\theta + EI_{\eta\xi} w''^2 \cos 2\theta \right.$$

$$- \left(\frac{EB_2}{2} \cos \theta - \frac{EB_3}{2} \sin \theta\right) w''\phi'^2$$

$$+ EA\frac{c^2}{8} w''\phi'^2 \left(e_\eta \cos \theta - e_\xi \sin \theta\right) \Bigg\} \delta\phi$$

$$+ \left\{ \left(\frac{EB_1}{2} - EAk_A^2 \frac{c^2}{4} + EA\frac{c^4}{32}\right) \phi'^3 \right.$$

$$- \left(EB_2 \sin \theta + EB_3 \cos \theta\right) w''\phi' + GJ\phi'$$

$$+ EA\frac{c^2}{4} w''\phi' \left(e_\eta \sin \theta + e_\xi \cos \theta\right) \Bigg\} \delta\phi' \quad (15)$$

The double-underlined, dashed-underlined, and wave-underlined terms of Eq. (15) were not always retained in previous studies for various reasons. The double-underlined terms were sometimes considered as higher-order terms, for rotor blades experiencing small angles of elastic twist. Note that Hodges and Dowell [7] also identified them as higher-order terms but mentioned their importance for the torsion equation of motion of blades with low torsional stiffness. The terms with dashed-underline must be kept for arbitrary nonsymmetric cross sections. Finally, the wave-underlined terms are associated with the foreshortening of the blade due to the trapeze effect.

Additionally, a localized pinching of the rotor blades was observed during operation, due to the clamping force of the blade grips (see Fig. 1b). This pinching resulted in a local discontinuity in flap bending stiffness at the root and was also seen in measurements of the flap bending deflection. To model these observations, a discrete torsional flapping spring was included at the root of the flexible rotor blade, and its effect was included in the strain energy as follows:

$$\delta V_{\text{sp}} = k_\beta w'(x_0)\delta w'(x_0) \quad (16)$$

where k_β is the torsional flapping spring stiffness.

4. Time-Invariant Kinetic Energy

Next, the variation of the kinetic energy can be written as

$$(\delta T)_b = \int_R \iint_A \rho \frac{d r_1}{dt} \cdot \delta\left(\frac{d r_1}{dt}\right) d\eta \, d\xi \, dx \quad (17)$$

where

$$\delta\left(\frac{d r_1}{dt}\right) = \begin{Bmatrix} \delta\dot{x}_1 - \Omega\delta y_1 \\ \delta\dot{y}_1 + \Omega\delta x_1 \\ \delta\dot{z}_1 \end{Bmatrix} \quad (18)$$

Expanding the scalar product and retaining only the time-invariant terms, we can obtain the variation of time-invariant kinetic energy as

$$(\delta T_0)_b = \int_R \iint_A \rho\Omega^2(x_1\delta x_1 + y_1\delta y_1) d\eta \, d\xi \, dx \quad (19)$$

Integrating over the blade cross section and introducing the cross-sectional constants defined in Table A1, we get

$$(\delta T_0)_b = \int_{x_0}^{R} \left\{ w' \left(\int_x^R -m_0 \Omega^2 \chi \, d\chi \right) \right.$$
$$- m_0 \Omega^2 x \left(d_\eta \sin\theta + d_\xi \cos\theta \right) \right\} \delta w'$$
$$+ \left\{ - m_0 \Omega^2 x w' \left(d_\eta \cos\theta - d_\xi \sin\theta \right) \right.$$
$$- m_0 \Omega^2 \frac{1}{2} \left(k_{m_\xi}^2 - k_{m_\eta}^2 \right) \sin 2\theta - m_0 \Omega^2 k_{m_{\eta\xi}}^2 \cos 2\theta \right\} \delta\phi$$
$$+ \left\{ \frac{c^2}{4} \phi' \left(\int_x^R -m_0 \Omega^2 \chi \, d\chi \right) \right\} \delta\phi' \qquad (20)$$

Terms resulting from asymmetry of the blade cross section are identified by a dashed-underline and those associated with the trapeze effect are wave-underlined.

5. Gravitational Potential Energy

The contribution of the gravitational potential energy to the steady-state deformation of a rotor blade is small compared to the deformation due to centrifugal and aerodynamic forces. Nevertheless, the gravitational energy plays a major role during the deployment of an extremely flexible rotor at startup. Therefore, it was included in the present analysis. The definition of the variation of gravitational potential energy is

$$(\delta V_g)_b = \int_R \iint_A \rho g \delta r_1 \cdot Z_I \qquad (21)$$

Using Eq. (10) and the section integral constants defined in Table A1, we obtain

$$(\delta V_g)_b = \int_{x_0}^{R} m_0 g \delta w - \{m_0 g w' (d_\eta \sin\theta + d_\xi \cos\theta)\} \delta w'$$
$$+ \left\{ m_0 g \left(1 - \frac{w'^2}{2} \right) (d_\eta \cos\theta - d_\xi \sin\theta) \right\} \delta\phi \qquad (22)$$

6. Kinetic and Gravitational Potential Energies of the Tip Mass

To complete the structural model, the kinetic energy and gravitational potential energy arising from the presence of the tip mass must be included. The tip mass was modeled as a uniform rod of mass per unit length m_T, secured to the tip of the blade and oriented with an index angle θ_{ind} relative to the chord of the blade (Fig. 7a). The distances between the tip mass attachment point and the elastic axis are η_T and ξ_T along the η and ξ axes, respectively (Fig. 7b).

The position vector $\boldsymbol{r}_{1m}$ of a particle along the longitudinal axis of the tip mass was deduced from the expression found for $\boldsymbol{r}_1$ [Eq. (10)], in which we substituted

$$x = R \qquad (23)$$
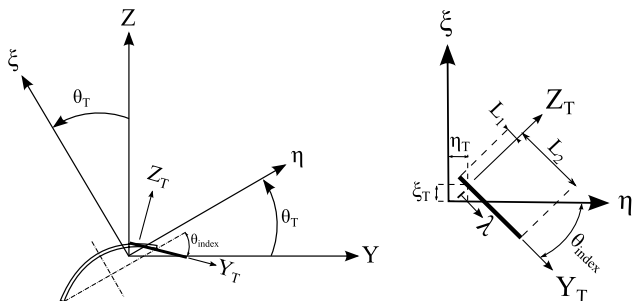
a) Position of the tip mass on the flexible blade BP

b) System of axis attached to the tip mass

Fig. 7   Position and orientation of the tip mass for the flexible-blade BP.

$$\eta = \eta_T + \lambda \cos(\theta_{\text{ind}}) \qquad (24)$$

$$\xi = \xi_T - \lambda \sin(\theta_{\text{ind}}) \qquad (25)$$

Then, the time-invariant variation of kinetic energy of the tip mass is given by

$$(\delta T_0)_m = \int_{-L_1}^{L_2} \iint_{A_m} \rho_m \Omega^2 (x_{1m}\delta x_{1m} + y_{1m}\delta y_{1m}) \, dA_m \, d\lambda \qquad (26)$$

where A_m and ρ_m are the cross-sectional area and the density of the tip mass, respectively. Taking the variations of the position vector r_{1m}, assuming λ, η_T, and ξ_T to be of order ϵ, and retaining first- and second-order terms only, we get

$$(\delta T_0)_m = \int_{x_0}^{R} \left\{ - m_T \Omega^2 R \left(w'\delta w' + \frac{c^2}{4} \phi'\delta\phi' \right) \right\} dx$$
$$- m_T \Omega^2 R \left\{ \eta_T \sin\theta_R + \xi_T \cos\theta_R \right.$$
$$+ \frac{L_2 - L_1}{2} \sin(\theta_R - \theta_{ind}) \right\} \delta w'_R$$
$$- m_T \Omega^2 \left\{ R w'_R \left(\eta_T \cos\theta_R - \xi_T \sin\theta_R \right. \right.$$
$$+ \frac{L_2 - L_1}{2} \cos(\theta_R - \theta_{ind}) \right)$$
$$+ \left(\frac{\eta_T^2}{2} - \frac{\xi_T^2}{2} \right) \sin 2\theta_R + \eta_T \xi_T \cos 2\theta_R$$
$$+ \frac{L_1^3 + L_2^3}{6(L_1 + L_2)} \sin 2(\theta_R - \theta_{ind})$$
$$+ \frac{L_2 - L_1}{2} \left(\eta_T \sin(2\theta_R - \theta_{ind}) + \xi_T \cos(2\theta_R - \theta_{ind}) \right) \right\} \delta\phi_R \qquad (27)$$

The subscript $(\cdot)_R$ indicates that the quantity is evaluated at the tip of the blade.

Finally, the variation of gravitational potential energy of the tip mass is

$$(\delta V_g)_m = \int_{L_1}^{L_2} \iint_{A_m} \rho_m g (\delta r_{1m} \cdot Z_I)$$
$$= m_T g \delta w_R - m_T g w'_R \left(\eta_T \sin\theta_R + \xi_T \cos\theta_R \right.$$
$$+ \frac{L_2 - L_1}{2} \sin(\theta_R - \theta_{ind}) \right) \delta w'_R$$
$$+ m_T g \left(1 - \frac{w'^2_R}{2} \right) \left(\eta_T \cos\theta_R - \xi_T \sin\theta_R \right.$$
$$+ \frac{L_2 - L_1}{2} \cos(\theta_R - \theta_{ind}) \right) \delta\phi_R \qquad (28)$$

C. Aerodynamic Model

A quasi-static model was used to calculate the aerodynamic forces on the rotor blade. The model was based on blade element momentum theory (BEMT) with a table lookup for the lift coefficients. These data were obtained from published literature of the low-Reynolds-number lift coefficients of a thin circular-arc airfoil [22]. The constant moment coefficient C_{m_0} was also included. Figure 8 shows the aerodynamic forces (lift and drag) and moment applied to a blade cross section. The local angle of attack α was defined as the angle between the chord of the airfoil and the resultant velocity vector U and is a function of the radial position along the blade. The induced angle of attack $\psi(x)$ was calculated using BEMT. Consequently, the local angle of attack was
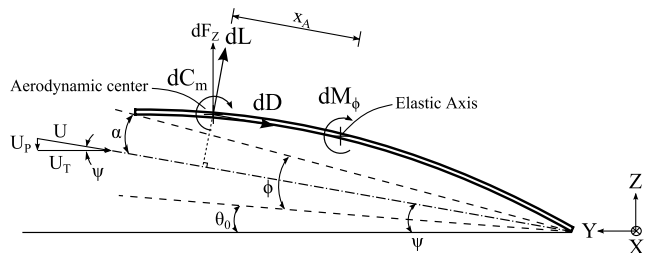
Fig. 8 Aerodynamic forces on a blade cross section.

$$\alpha(x) = \theta_0 + \phi(x) - \psi(x) \tag{29}$$

Because the air velocity of the blade section perpendicular to the disk plane (U_P) is small compared to the air velocity tangent to the disk plane (U_T), the induced angle of attack ψ is small. In addition, by projecting the aerodynamic forces on the Z axis, the virtual work done by the aerodynamic forces on the blade section can be written as

$$\delta W_a = \int_R dF_z \delta w + dM_\phi \delta\phi$$
$$= \int_{x_0}^R \left\{ \frac{1}{2}\rho_{\text{air}}(\Omega x)^2 c C_l \right\} \delta w$$
$$+ \left\{ \frac{1}{2}\rho_{\text{air}}(\Omega x)^2 c x_A C_l + \frac{1}{2}\rho_{\text{air}}(\Omega x)^2 c^2 C_{m_0} \right\} \delta\phi \tag{30}$$

where x_A is the distance between the aerodynamic center and the elastic axis. In summary, the final formulation of the blade equation of motion in integral form is given in Appendix B.

D. Solution Procedure

The equations of motion derived as described previously were solved using a finite-element formulation. The rotor blade was discretized into 20 beam elements. Each beam element had seven degrees of freedom, distributed over three nodes (Fig. 9), which forms an elemental vector of generalized coordinates

$$q_i = \{w_1 w_1' w_3 w_3' \phi_1 \phi_2 \phi_3\}^T \tag{31}$$

Assembly of the elemental vectors of generalized coordinates yields the global displacement vector

$$u = \{w_1 w_1' w_3 w_3' w_5 w_5' \cdots \phi_1 \phi_2 \phi_3 \phi_4 \phi_5 \cdots\}^T \tag{32}$$

Between the elements, there is continuity of displacement and slope for the flap bending deflection as well as continuity of displacement for the twist angles. Using appropriate shape functions (Hermite cubic and Lagrange quadratic polynomials for the bending and twist degrees of freedom, respectively), we can express the bending displacement $w(x)$ and twist $\phi(x)$ over one element as a function of the generalized coordinates as follows:

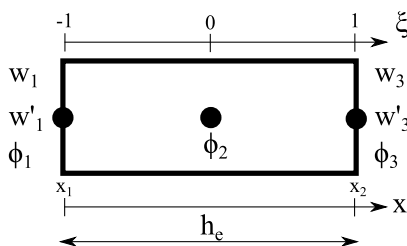$$w(x) = \sum_{i=1}^2 w_i H_i^0(x) + w_i' H_i^1(x) \tag{33}$$

Fig. 9 Finite element.

$$\phi(x) = \sum_{j=1}^3 \phi_j L_j(x) \tag{34}$$

Upon discretization, the steady-state formulation of the extended Hamilton's principle [Eq. (2)] becomes

$$\sum_{i=1}^N (\delta T_{0i} - \delta U_i - \delta V_{gi} + \delta W_{ai})_b + (\delta T_0 - \delta V_g)_m = 0 \tag{35}$$

where N is the total number of elements, and the subscript i indicates the contribution of the ith element to the total energy. Arbitrariness of the δq_i in Eq. (35) leads to the formation of a system of M nonlinear equations, where M is the number of degrees of freedom. This system of equations can be solved iteratively by the Newton–Raphson method.

At the ith iteration, substituting the global displacement vector u^i in the system of nonlinear equations leads to a residue vector R^i on the right-hand side. Taking the partial derivatives of the residue vector with respect to the displacement vector u^i, we obtain the Jacobian matrix

$$K^i = \frac{\partial R^i}{\partial u^i} \tag{36}$$

In the present model, the components of the Jacobian matrix were calculated analytically, which led to better stability of the algorithm. Then, the Newton–Raphson method determines the displacement vector for the next iteration as

$$u^{i+1} = u^i - \lambda^i (K^{-1} R)^i \tag{37}$$

where λ^i is a constant calculated using a line-search algorithm [23].

V. Results and Discussion

The steady-state aeroelastic analysis was first validated with experimental measurements of the rotor loads, the spanwise flap bending, and the twist distribution of the rotor blade. The validated analysis was then used to explore the effect of refined torsional modeling, specifically, the contribution of the terms associated with the trapeze effect.

A. Correlation of the Model with Experiment

The extremely flexible rotor spinning at 1500 rpm was tested over a range of collective pitch angles from 0 to 25 deg. The thrust generated by the rotor and measured by the load cell is plotted as a function of the pitch angle in Fig. 10. It can be seen that the thrust coefficient computed from the experimental data was well predicted by the present analysis. The flexible rotor generates a blade loading (C_T/σ) equal to 0.203 at a high collective pitch angle of approximately 30 deg.
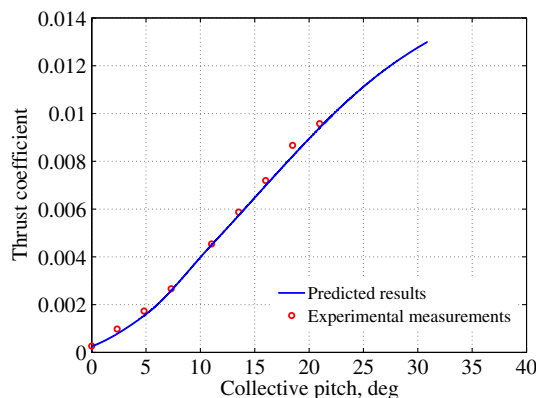

Fig. 10 Predicted and measured thrust coefficient of the extremely flexible rotor, at 1500 rpm.

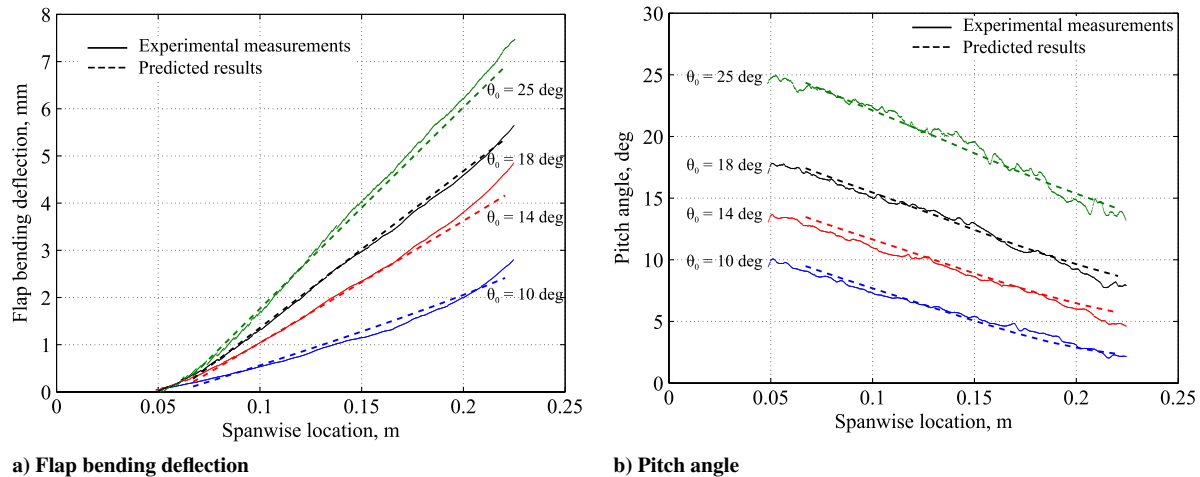**a) Flap bending deflection**   **b) Pitch angle**

Fig. 11   Predicted and measured deformations of the extremely flexible rotor blade, at 1200 rpm.

Furthermore, the spanwise distribution of flap bending as well as spanwise twist of the rotor blades spinning at 1200 rpm were extracted from the DIC measurements and are shown in Figs. 11a and 11b. Also shown for comparison are the deformations predicted by the steady-state aeroelastic analysis.

We observe that there is very good correlation between the experimental measurements of pitch and the analytical predictions. In addition, we can see that that the slope of the flap bending deflection, in the measured data, is not zero at the root. This observation motivated the inclusion of a flapping spring at the blade root. The value of this spring stiffness was adjusted so that the predicted flap bending deformation at the lowest collective pitch matched the measurements; this value was then used for the predictions at the other collective pitch angles. There is some discrepancy between measurements and analytical predictions of bending deflection near the blade tip, where the tip mass is located. The chordwise offset of the tip mass from the elastic axis creates significant bending moments in the lead–lag direction. To properly capture this effect, a lead–lag degree of freedom must be added to the analysis; this refinement is the subject of future work. In addition, it should be noted that, because of the low structural stiffness of the rotor blade, it is likely that the deformations lead to a modification of the airfoil cross section, particularly of the airfoil camber. Consequently, these chordwise deformations affect the aerodynamic coefficients as well as the flap bending deflection. The addition of a lead–lag degree of freedom to the analysis along with correlations with measurements of chordwise deformations will be investigated in the future. Based on the comparison between experimental measurements and predictions, we concluded that the analytical model was validated and could be used to investigate the aspects of refined modeling of the torsional deformation of unconventional flexible blades.

B.   Importance of Refined Torsion Modeling

The trapeze effect plays a minor role in conventional analyses developed for torsionally stiff rotor blades. Additionally, it is typically appropriate to assume the elastic twist to be $O\epsilon$) (same as the normalized flap bending deflection, w/R). However, in the present analysis, the trapeze effect is explicitly included, and the elastic twist is assumed to be $O(1)$ to capture the effect of low torsional stiffness. The effect of adding these larger torsional deformations in the present analysis is investigated. In addition, the lowest value of torsional stiffness that can be modeled by an analysis omitting these additional terms is explored.

1.   Influence of the Trapeze Effect

The trapeze effect acting on a twisted beam with axial loading is responsible for a torsional moment (the trapeze moment) that tends to restore the beam to its untwisted position. In the case of a rotating blade, the axial loading is the centrifugal force. The propeller moment acting on a rotor blade tends to align the rotor blade chord with the plane of rotation. Therefore, in the case of a torsionally soft rotor blade with a positive root pitch, the propeller moment at the blade tip (nose-down) acts in opposition to the trapeze moment (nose-up, untwisting the blade).

To quantify the magnitude of the trapeze moment compared to the other pitching moments acting on a torsionally soft rotor blade, each term related to the trapeze effect in the equations of motion, identified by a wave-underline in Eqs. (15,20,27), was removed, and the resulting flap bending and twist deformations were calculated. Figures 12a and 12b show the contribution of the trapeze effect terms on the deformations of the flexible blade rotating at 1200 rpm. The spanwise distribution of twist shows larger negative (nose-down) pitch angles for the case where the trapeze moment is ignored. As the
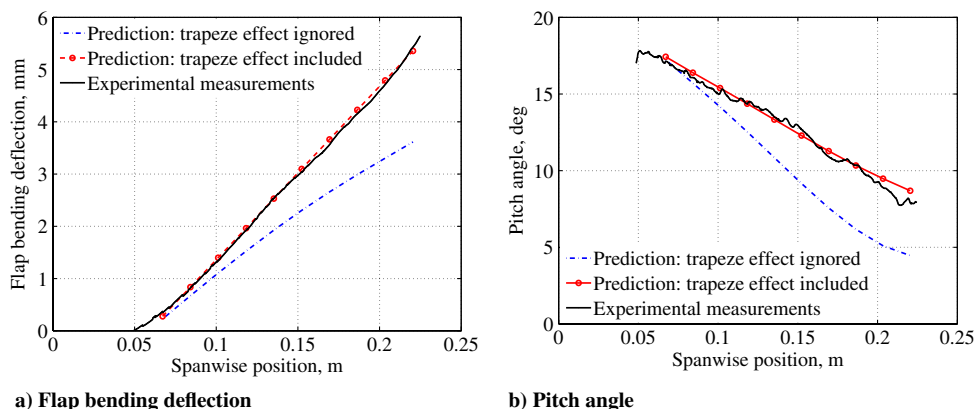

a) Flap bending deflection   **b) Pitch angle**

Fig. 12   Influence of the trapeze effect on the deformations of an extremely flexible rotor blade, at 1200 rpm, $\theta_0 = 18$ deg.

a) Influence of the trapeze effect terms contained in the kinetic energy vs. the strain energy

b) Influence of the trapeze effect terms contained in the tip mass kinetic energy vs. the blade kinetic energy
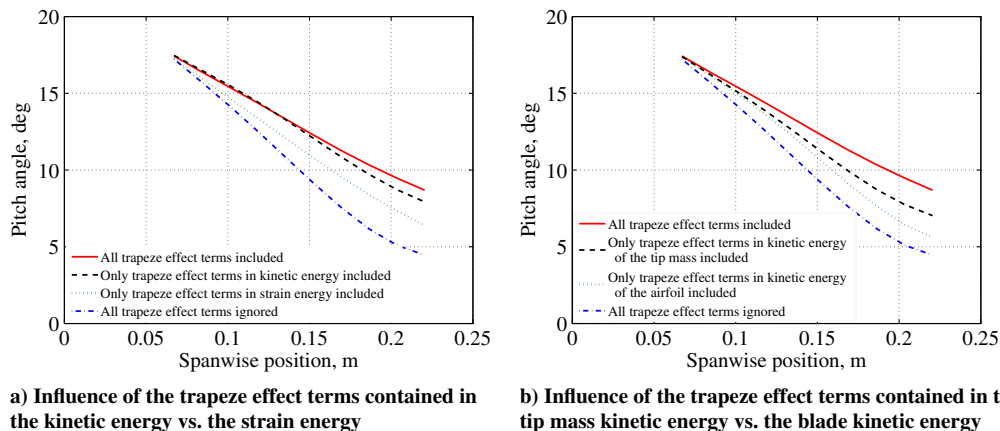
Fig. 13 Investigation of the influence of terms corresponding to the trapeze effect on the twist deformation of an extremely flexible rotor blade, at 1200 rpm, $\theta_0 = 18$ deg.

trapeze moment is neglected, its effect of acting against the negative propeller moment and negative aerodynamic pitching moment disappears, and the resultant twist along the blade is greater. The effect is also seen on the flap bending curves; when the trapeze moment is considered, the magnitude of the nose-down blade twist is decreased, and hence the angle of attack at each section is larger leading to higher lift and greater flap bending deflection.

To better understand the origin of the trapeze effect, the contribution of each term arising from this effect in the equations of motion was investigated. Four cases were studied, each case separately including a trapeze effect term in the equations of motion. The terms included in each case were one strain energy term and three kinetic energy terms: 1) coupling terms between torsion and centrifugal stress in the strain energy from Eq. (15); 2) coupling terms between torsion and centrifugal stress in the kinetic energy of the tip mass from Eq. (27); 3) coupling terms between torsion and centrifugal stress in the kinetic energy of the airfoil from Eq. (20); and 4) coupling terms between torsion and total centrifugal stress (cases 1 and 2).

From Fig. 13a, it can be seen that the main contribution to the trapeze moment comes from the trapeze effect terms included in the kinetic energy. It is interesting to note that because of the nonlinear nature of the trapeze effect, the solution including all the trapeze effect terms is not equal to the sum of the solutions where the trapeze effect terms are included individually. In addition, it can be seen in Fig. 13b that the trapeze restoring pitching moment acting on the tip mass is larger than that acting on the blade. Finally, we see that all the trapeze effect terms must be included to obtain an accurate prediction of the spanwise twist distribution.

2. Influence of the Higher-Order Twist Terms

In the present analysis, the twist angles were assumed to be arbitrarily large, or in other words, $O(1)$. This assumption led to additional terms in the equations of motion, double-underlined in Eq. (15). The importance of the double-underlined terms is such that, by neglecting them and linearizing the trigonometric functions for small angles ϕ, the analysis does not converge for the blade parameters shown in Table 1. Mathematically, this lack of convergence means that the equivalent stiffness matrix was ill-conditioned, and a solution could not be calculated by the solver. Physically, this lack of convergence means that the equations of motion with omitted terms do not capture the behavior of an extremely flexible rotor. In fact, it was verified that the analysis without the double-underlined terms was only able to converge for normalized stiffnesses of

$$\frac{EI_\eta}{m_0\Omega^2 R^4} = 2.70 \times 10^{-1} \tag{38}$$

$$\frac{EI_\xi}{m_0\Omega^2 R^4} = 7.12 \times 10^1 \tag{39}$$

$$\frac{GJ}{m_0\Omega^2 R^4} = 2.66 \times 10^1 \tag{40}$$

These values correspond to a blade of the same geometry as the blade described in Table 1 but fabricated out of aluminum. We conclude that the assumption of small elastic twist angle is reasonable for a relatively stiff rotor blade but leads to a singular problem for the computation of the deformation of an extremely flexible rotor blade.

VI. Conclusions

An analytical model of the torsional deformation of an extremely flexible rotor in hover was presented. The model included flap bending and twist degrees of freedom. Compared to typical analyses based on ordering schemes and derived for conventional rotors, the present model included additional terms related to the presence of large elastic twist angles. First, the magnitude of the elastic twist was assumed to be of one order of magnitude greater than the normalized flap bending deflection. Second, the foreshortening of the twisted rotor blade resulting from the trapeze effect was included to the position vector explicitly.

The nonlinear coupled equations of motion were derived using the extended Hamilton's principle and were solved using a finite-element approach. Nonlinear terms were linearized using a Newton–Raphson scheme and were incorporated into the stiffness matrix and force vector. The predictions of the flap bending and twist deformations of a flexible rotor blade rotating at 1200 rpm showed good agreement with experimental measurements obtained by stereoscopic DIC.

Then, an extensive investigation on the importance of the trapeze effect in the aeroelastic modeling of blade with low torsional stiffness was conducted. It was found that omitting the terms due to trapeze effect led to a 50% error in the computation of the blade-tip pitch angle. It was also shown that, among the terms arising from the trapeze effect, kinetic energy terms were predominant over the strain energy terms.

Finally, to verify the large twist angle assumption made for this analysis, a model derived for small angle and neglecting all higher-order twist terms was developed. This model could not converge or find steady-state equilibrium positions for a rotor blade with normalized torsional stiffness of the order of 10^{-3}. This observation confirmed the necessity of considering elastic twist angles as arbitrarily large.

Future plans involve the refinement of the analysis by the addition of lead–lag degrees of freedom. The aeroelastic model will also be expanded to include the dynamic analysis of extremely flexible rotors. The objective of the dynamic analysis will be to analytically identify stability boundaries and correlate the results with experimental observations.

Appendix A:

Table A1   Cross-Sectional Integral Constants

$\int_A \mathrm{d}\eta\,\mathrm{d}\xi = A$	$\int_A \eta^2\,\mathrm{d}\eta\,\mathrm{d}\xi = I_\xi$	$\int_A (\eta^2 + \xi^2)^2\,\mathrm{d}\eta\,\mathrm{d}\xi = B_1$
$\int_A \eta\,\mathrm{d}\eta\,\mathrm{d}\xi = Ae_\eta$	$\int_A \xi^2\,\mathrm{d}\eta\,\mathrm{d}\xi = I_\eta$	$\int_A \eta(\eta^2 + \xi^2)\,\mathrm{d}\eta\,\mathrm{d}\xi = B_2$
$\int_A \xi\,\mathrm{d}\eta\,\mathrm{d}\xi = Ae_\xi$	$\int_A \eta\xi\,\mathrm{d}\eta\,\mathrm{d}\xi = I_{\eta\xi}$	$\int_A \xi(\eta^2 + \xi^2)\,\mathrm{d}\eta\,\mathrm{d}\xi = B_3$
	$\int_A (\eta^2 + \xi^2)\,\mathrm{d}\eta\,\mathrm{d}\xi = J = Ak_A^2$	
$\int_A \rho\,\mathrm{d}\eta\,\mathrm{d}\xi = m_0$	$\int_A \rho\eta^2\,\mathrm{d}\eta\,\mathrm{d}\xi = m_0 k_{m_\xi}^2$	$\int_A \rho(\eta^2 + \xi^2)\,\mathrm{d}\eta\,\mathrm{d}\xi = m_0 k_m^2$
$\int_A \rho\eta\,\mathrm{d}\eta\,\mathrm{d}\xi = m_0 d_\eta$	$\int_A \rho\xi^2\,\mathrm{d}\eta\,\mathrm{d}\xi = m_0 k_{m_\eta}^2$	
$\int_A \rho\xi\,\mathrm{d}\eta\,\mathrm{d}\xi = m_0 d_\xi$	$\int_A \rho\eta\xi\,\mathrm{d}\eta\,\mathrm{d}\xi = m_0 k_{m_{\eta\xi}}$	

Appendix B: Steady-State Equilibrium Equation for an Extremely Flexible Blade with Tip Mass

$$(\delta T_0 - \delta U - \delta V_g + \delta W_a)_b + (\delta T_0 - \delta V_g)_m = 0 \qquad (B1)$$

where

$$
\begin{aligned}
(\delta T_0)_b = \int_{x_0}^{R} &\left\{ w'\left(\int_x^R -m_0\Omega^2\chi\,\mathrm{d}\chi \right) \right.\\
&- m_0\Omega^2 x(d_\eta \sin\theta + d_\xi \cos\theta)\}\delta w'\\
&+ \left\{ -m_0\Omega^2 xw'(d_\eta \cos\theta - d_\xi \sin\theta) \right.\\
&- m_0\Omega^2 \frac{1}{2}(k_{m_\xi}^2 - k_{m_\eta}^2)\sin 2\theta - m_0\Omega^2 k_{m_{\eta\xi}}\cos 2\theta \bigg\}\delta\phi\\
&+ \left. \left\{ \frac{c^2}{4}\phi'\left(\int_x^R -m_0\Omega^2\chi\,\mathrm{d}\chi \right) \right\}\delta\phi' \right\} \qquad (B2)
\end{aligned}
$$

$$
\begin{aligned}
(\delta U)_b = \int_{x_0}^{R} &\left\{ (EI_\xi \sin^2\theta + EI_\eta \cos^2\theta + EI_{\eta\xi}\sin 2\theta)w'' \right.\\
&- \left(\frac{EB_2}{2}\sin\theta + \frac{EB_3}{2}\cos\theta \right)\phi'^2\\
&+ EA\frac{c^2}{8}\phi'^2(e_\eta \sin\theta + e_\xi \cos\theta) \bigg\}\delta w''\\
&+ \left\{ \frac{1}{2}(EI_\xi - EI_\eta)w''^2\sin 2\theta + EI_{\eta\xi}w''^2\cos 2\theta \right.\\
&- \left(\frac{EB_2}{2}\cos\theta - \frac{EB_3}{2}\sin\theta \right)w''\phi'^2\\
&+ EA\frac{c^2}{8}w''\phi'^2(e_\eta \cos\theta - e_\xi \sin\theta) \bigg\}\delta\phi\\
&+ \left\{ \left(\frac{EB_1}{2} - EAk_A^2\frac{c^2}{4} + EA\frac{c^4}{32} \right)\phi'^3 \right.\\
&- (EB_2 \sin\theta + EB_3 \cos\theta)w''\phi'' + GJ\phi''\\
&+ EA\frac{c^2}{4}w''\phi'(e_\eta \sin\theta + e_\xi \cos\theta) \bigg\}\delta\phi' \qquad (B3)
\end{aligned}
$$

$$
\begin{aligned}
(\delta V_g)_b = m_0 g \int_{x_0}^{R} &\delta w - \{w'(d_\eta \sin\theta + d_\xi \cos\theta)\}\delta w'\\
&+ \left\{ \left(1 - \frac{w'^2}{2} \right)(d_\eta \cos\theta - d_\xi \sin\theta) \right\}\delta\phi \qquad (B4)
\end{aligned}
$$

$$
\begin{aligned}
(\delta W_a)_b = \int_{x_0}^{R} &\left\{ \frac{1}{2}\rho_{\mathrm{air}}(\Omega x)^2 cC_l \right\}\delta w\\
&+ \left\{ \frac{1}{2}\rho_{\mathrm{air}}(\Omega x)^2 cx_A C_l + \frac{1}{2}\rho_{\mathrm{air}}(\Omega x)^2 c^2 C_{m_0} \right\}\delta\phi \qquad (B5)
\end{aligned}
$$

$$
\begin{aligned}
(\delta T_0)_m = &\left(\int_{x_0}^{R} -m_T\Omega^2 R\left\{ w'\delta w' + \frac{c^2}{4}\phi'\delta\phi'\} \,\mathrm{d}x \right)\right.\\
&- m_T\Omega^2 R\left\{ \eta_T \sin\theta_R + \xi_T \cos\theta_R + \frac{L_2 - L_1}{2}\sin(\theta_R - \theta_{\mathrm{ind}}) \right\}\delta w_R'\\
&- m_T\Omega^2 \left\{ Rw_R'\left(\eta_T \cos\theta_R - \xi_T \sin\theta_R + \frac{L_2 - L_1}{2}\cos(\theta_R - \theta_{\mathrm{ind}}) \right) \right.\\
&+ \left(\frac{\eta_T^2}{2} - \frac{\xi_T^2}{2} \right)\sin 2\theta_R + \eta_T\xi_T \cos 2\theta_R + \frac{L_1^3 + L_2^3}{6(L_1 + L_2)}\sin 2(\theta_R - \theta_{\mathrm{ind}})\\
&+ \frac{L_2 - L_1}{2}(\eta_T \sin(2\theta_R - \theta_{\mathrm{ind}}) + \xi_T \cos(2\theta_R - \theta_{\mathrm{ind}})) \bigg\}\delta\phi_R \qquad (B6)
\end{aligned}
$$

$$
\begin{aligned}
(\delta V_g)_m = m_T g &\left\{ \delta w_R - w_R'(\eta_T \sin\theta_R + \xi_T \cos\theta_R \right.\\
&+ \frac{L_2 - L_1}{2}\sin(\theta_R - \theta_{\mathrm{ind}}))\delta w_R'\\
&+ \left(1 - \frac{w_R'^2}{2} \right)(\eta_T \cos\theta_R - \xi_T \sin\theta_R + \frac{L_2 - L_1}{2}\cos(\theta_R - \theta_{\mathrm{ind}}))\delta\phi_R \bigg\} \qquad (B7)
\end{aligned}
$$

Note that $\theta(x)$ is the sum of the collective pitch and the elastic twist angle:

$$\theta(x) = \theta_0 + \phi(x) \qquad (B8)$$

References

[1] Pines, D. J., and Bohorquez, F., "Challenges Facing Future Micro-Air Vehicle Development," *Journal of Aircraft*, Vol. 43, No. 2, 2006, pp. 290–305.
doi:10.2514/1.4922

[2] Chopra, I., "Hovering Micro Air Vehicles: Challenges and Opportunities," *Proceedings of the International Forum on Rotorcraft Multidisciplinary Technology*, Seoul, South Korea, Oct. 2007.

[3] Bohorquez, F., Samuel, P., Sirohi, J., Pines, D., Rudd, L., and Perel, R., "Design, Analysis and Hover Performance of a Rotary Wing Micro Air Vehicle," *Journal of the American Helicopter Society*, Vol. 48, No. 2, 2003, pp. 80–90.
doi:10.4050/JAHS.48.80

[4] Sicard, J., and Sirohi, J., "Experimental Study of an Extremely Flexible Rotor for Microhelicopters," *Journal of Aircraft*, Vol. 49, No. 5, 2012, pp. 1306–1314.
doi:10.2514/1.C031643

[5] Hein, B. R., and Chopra, I., "Hover Performance of a Micro Air Vehicle: Rotors at Low Reynolds Number," *Journal of the American Helicopter Society*, Vol. 52, No. 3, 2007, pp. 254–262.
doi:10.4050/JAHS.52.254

[6] Houbolt, J. C., and Brooks, G. W., "Differential Equations of Motion for Combined Flapwise Bending, Chordwise Bending, and Torsion of Twisted Nonuniform Rotor Blades," NACA TN-3905, Feb. 1957.

[7] Hodges, D. H., and Dowell, E. H., "Nonlinear Equations of Motion for the Elastic Bending, and Torsion of Twisted Nonuniform Rotor Blades," NASA TN-D-7818, Dec. 1974.

[8] Kaza, K. R. V., and Kvaternik, R. G., "Nonlinear Aeroelastic Equations for Combined Flapwise Bending, Chordwise Bending, Torsion and Extension of Twisted Nonuniform Rotor Blades in Forward Flight," NASA TM-74059, Aug. 1977.

[9] Rosen, A., and Friedmann, P. P., "Nonlinear Equations of Equilibrium for Elastic Helicopter or Wind Turbine Blades Undergoing Moderate Deformation," NASA CR-159478, Dec. 1978.

[10] Hodges, D. H., "A Mixed Variational Formulation Based on Exact Intrinsic Equations for Dynamics of Moving Beams," *International Journal of Solids and Structures*, Vol. 26, No. 11, 1990, pp. 1253–1273.
doi:10.1016/0020-7683(90)90060-9

[11] Hodges, D. H., "Geometrically Exact, Intrinsic Theory for Dynamics of Curved and Twisted Anisotropic Beams," *AIAA Journal*, Vol. 41, No. 6, 2003, pp. 1131–1137.
doi:10.2514/2.2054

[12] Bauchau, O. A., and Kang, N. K., "A Multibody Formulation for Helicopter Structural Dynamic Analysis," *Journal of the American Helicopter Society*, Vol. 38, No. 2, 1993, pp. 3–14.
doi:10.4050/JAHS.38.3

[13] Datta, A., Nixon, M., and Chopra, I., "Review of Rotor Loads Prediction with the Emergence of Rotorcraft CFD," *Journal of the American Helicopter Society*, Vol. 52, No. 4, 2007, pp. 287–317.
doi:10.4050/JAHS.52.287

[14] Johnson, W., "Milestones in Rotorcraft Aeromechanics," NASA TP-2011-215971, May 2011.

[15] Goldman, R. L., "Some Observations on the Dynamic Behavior of Extremely Flexible Rotor Blades," *Proceedings of the 28th Annual Meeting of the IAS*, Inst. of the Aeronautical Sciences, New York, Jan. 1960; also Paper 1960-44.

[16] Winston, M. M., "An Investigation of Extremely Flexible Lifting Rotors," NASA TN-D-4465, April 1968.

[17] Winston, M. M., "A Hovering Investigation of an Extremely Flexible Lifting Rotor," NASA TN-D-4820, Oct. 1968.

[18] Sirohi, J., and Lawson, M. S., "Measurement of Helicopter Rotor Blade Deformation Using Digital Image Correlation," *Optical Engineering*, Vol. 51, No. 4, April 2012, pp. 043603-1–043603-8.
doi:10.1117/1.OE.51.4.043603

[19] Sicard, J., and Sirohi, J., "Measurement of the Deformation of an Extremely Flexible Rotor Using Digital Image Correlation," *Measurement Science and Technology*, Vol. 24, No. 6, 2013, Paper 065203.
doi:10.1088/0957-0233/24/6/065203

[20] Hodges, D. H., *Nonlinear Composite Beam Theory*, Vol. 213, Progress in Astronautics and Aeronautics, AIAA, Reston, VA, 2006, pp. 15–16.

[21] Hodges, D. H., Ormiston, R. A., and Peters, D. A., "On the Nonlinear Deformation Geometry of Euler-Bernouilli Beams," NASA TP-1980-1566, April 1980.

[22] Simons, M., *Model Aircraft Aerodynamics*, Trans-Atlantic Publ., Philadelphia, 1999, p. 232.

[23] Flannery, B., Press, W., Teukolsky, S., and Vetterling, W., *Numerical Recipes in C*, Cambridge Univ. Press, New York, 1992, pp. 376–381.

W. Silva
Associate Editor